Journal of Applied Geophysics 135 (2016) 17–31

Contents lists available at ScienceDirect

Journal of Applied Geophysics

journal homepage: www.elsevier.com/locate/jappgeo

Application of the marine circular electric dipole method in high latitude Arctic regions using drifting ice floes

Vladimir Mogilatov [a,b], Mark Goldman [c], Marina Persova [d,*], Yury Soloveichik [d], Yulia Koshkina [d], Olga Trubacheva [d], Arkadiy Zlobinskiy [e]

[a] Institute of Petroleum Geology and Geophysics, Novosibirsk 630090, Russia
[b] Novosibirsk State University, Novosibirsk 630090, Russia
[c] University of Haifa, Haifa 31905, Israel
[d] Novosibirsk State Technical University, Novosibirsk 630073, Russia
[e] Scientific-Technical Company " ZaVeT-GEO", Novosibirsk 630102, Russia

ARTICLE INFO

Article history:
Received 18 September 2015
Received in revised form 15 July 2016
Accepted 23 August 2016
Available online 25 August 2016

Keywords:
Circular electric dipole
Drifting ice floes
Arctic

ABSTRACT

Theoretically, a circular electric dipole is a horizontal analogue of a vertical electric dipole and, similarly to the latter, it generates the unimodal transverse magnetic field. As a result, it demonstrates exceptionally high signal detectability and both vertical and lateral resolutions, particularly regarding thin resistive targets. The ideal circular electric dipole is represented by two concentric continuums of electrodes connected to different poles of the transmitter. In practice, the ideal dipole is adequately approximated by eight outer electrodes and one central electrode. The greatest disadvantage of circular electric dipoles stems from the necessity to provide perfectly symmetrical radial grounded lines with equal current in each line. In addition, relocating such a cumbersome system is very difficult on land and offshore. All these disadvantages might be significantly reduced in the proposed ice-borne system. The system utilizes drifting ice floes in high latitude Arctic regions as stable platforms for locating marine circular electric dipole transmitters, while the underlain ocean water is a perfect environment for grounding transmitter and receiver electrodes. Taking into account the limited size of drifting floes, mainly short offset methods can be applied from the surface. Among those, the proposed method is superior in providing sufficiently high signal detectability and resolution to delineate deep targets below very conductive ocean water and sub-seafloor sediments. Other existing methods, which are able to provide similar characteristics, utilize near bottom arrays and would be hard to employ in the presence of a thick ice cover.

1. Introduction

At present, high resolution geophysical exploration in the Arctic Ocean is limited to what a single ship might complete under open-water conditions in just 2–3 months a year. At the same time, the area permanently covered by ice is about four times the size of the Mediterranean Sea (Fig. 1). Only a few sporadic seismic profiles have been run in this area using icebreakers and drifting polar stations (e.g. Jokat, 2005; Poselov et al., 2012). Passive geophysical methods such as gravity, magnetic and magnetotelluric (MT) ones were widely applied in polar stations (e.g. Trofimov and Fonarev, 1976), but they only provided low resolution, general reconnaissance information.

As far as active geoelectric/geoelectromagnetic (GE/GM) methods are concerned, the most complicated problem that virtually prevents their efficient application in high latitude Arctic regions is the unfortunate combination of the deep (up to 4 km depth) very conductive ocean with a permanent ice cover. The deep conductive ocean plays the role of a practically impervious shield for all conventional active methods, which can be operated from the ice surface (e.g. ERT, LOTEM, CSAMT). On the other hand, the application of the leading marine method (CSEM), which is able to probe deep sub-seafloor targets (e.g. Constable and Srnka, 2007), is technically very difficult to impossible below permanent thick ice cover. Recently, a novel high resolution marine transient EM method based on the use of vertical electric dipoles/lines (VED/VEL) has been developed and tested in the sea (Holten et al., 2009; Helwig et al., 2013). The method called TEMP-VEL (Transient ElectroMagnetic Prospecting using Vertical Electric Lines) utilizes the unimodal TM-field and is therefore highly sensitive to resistive targets such as hydrocarbons and gas hydrates. However, due to particular vulnerability of the method regarding non-verticality of the dipoles (e.g. Goldman et al., 2015), its application on drifting ice floes seems questionable.

---

[*] Corresponding author at: Novosibirsk State Technical University, 20 Prospekt K. Marksa, Novosibirsk 630073, Russia.
E-mail address: persova@fpm.ami.nstu.ru (M. Persova).

http://dx.doi.org/10.1016/j.jappgeo.2016.08.007
0926-9851/

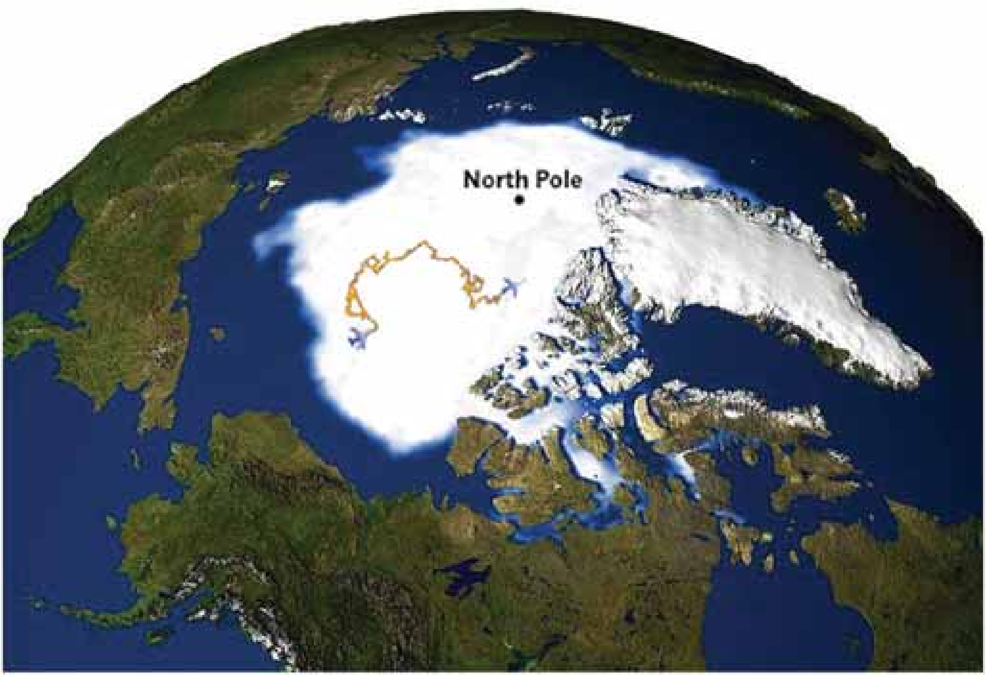

Fig. 1. NASA satellite image of the Arctic Ocean in July 2012. All the aquatic area covered by ice can be explored using proposed method. The choice of a suitable ice floe is crucial as it might be shrunk during summer time below the permissible dimensions of a few kilometers in diameter. An example of a travel path of a drifting ice floe: the longest path of the Russian polar station, NP-8(СП-8), during the period from March 1959 to March 1962. A total length of the path is 5976 km. The average drifting speed is approximately 5–6 km/day.

A method representing an alternative to existing GE/GEM methods under the abovementioned conditions is based on the use of a circular electric dipole (CED) transmitter and a horizontal electric dipole (HED) receiver, both located on the surface of a drifted ice floe. Such an array becomes possible because, contrary to conventional surface methods, CED signals are much less affected by the very conductive ocean water and sub-seafloor sediments and contrary to CSEM and TEMP-VEL, CED can be applied from the ice surface. Moreover, permanently drifting ice floes simplify the application of the CED as compared to “normal” on-land or open ocean conditions, because ice floes provide stable platforms for locating the CED transmitter, while the underlying sea water is highly suitable for grounding current electrodes. Above all, drifting ice floes ensure the cumbersome CED system moves along a profile. This allows applying CED for the first time not only as a semi-qualitative fixed transmitter mapping technique, but also as a quantitative high resolution sounding method.

Of course, the use of ice floes inevitably limits the range of tasks and possible targets because the proposed surveys can be carried out only along arbitrary and generally uncontrollable traverses. Nevertheless, obtaining high resolution geophysical information even along uncontrollable paths in high latitude Arctic regions, where such information is very limited to non-existent, is important. Such surveys can be primarily used for reconnaissance purposes and also for the exploration of hydrocarbons, gas hydrates, mineral deposits, etc. along the surveyed profiles.

Another, even more severe drawback, which is common for both CED and VED/VEL TDEM methods is an exceptional smallness of signal amplitudes at late times. Contrary to all conventional unimodal TE-methods and mixed TE/TM-methods, the signal amplitude in unimodal TM-methods exponentially decays at late times in the presence of insulating (practically, highly resistive) structures (Goldman et al., 2015). As a result, the unimodal TM-signals are smaller by orders of magnitude than those of unimodal TE and bimodal TE/TM-fields. However taking into account that this is a more technical than principal issue and the fact that the proposed marine CED is apparently the only possible high resolution EM technology in high latitude Arctic Ocean, its future application in this region is totally justified despite the above drawback.

2. Method

The concept of a circular electric dipole (CED) as a surface analogue of a vertical electric dipole (VED) was first introduced and theoretically substantiated by Mogilatov (1992). The method based on the use of CED and called vertical electric current soundings (VECS) has been further developed and practically realized by Mogilatov and Balashov (1996). The CED is a source that consists of a central electrode connected to one pole of a generator and (theoretically) a continuum of electrodes located along a circle and connected to another pole (Fig. 2a). In practice, the number of outer electrodes is finite and, in most cases, adequately represents the ideal CED, if it is ≥ 8 (Mogilatov and Balashov, 1996, Fig. 2b).

The successful application of a real CED requires providing very stable and equal currents in all legs of the transmitter dipole and a perfect symmetry in locating the legs. These are very challenging problems that are hard to solve on land due to topography and significantly different grounding conditions for outer electrodes. In addition, it is very difficult to relocate CED transmitters during on land surveys. As a result, at present, the CED system is practically realized as a fixed transmitter mapping tool only (Mogilatov and Balashov, 1996).

We propose here a novel application of moving CED transient systems by using drifting ice floes in high latitude Arctic regions. The proposed system includes a large CED transmitter located on a drifting ice floe with both central and outer electrodes immersed into the ocean water through the holes drilled in the floe (Fig. 3). For greater stability, the electrodes are firmly attached to the bottom of the floe. The allocation of all electrodes within highly uniform and very conductive sea water almost entirely resolves the inherent grounding problem of the existing on land CED system, and, moreover, the CED system relocates together with the drifting ice floe that allows mapping the sea bed along the drifting path of this ice floe.

This conceptual article is only aimed at describing most principal features and limitations of the proposed method, such as signal detectability, lateral resolution, sensitivity to geometrical errors, and current instability. More technical aspects, such as power requirements, types of electrodes and wires, and weights of generators and fuel, which are

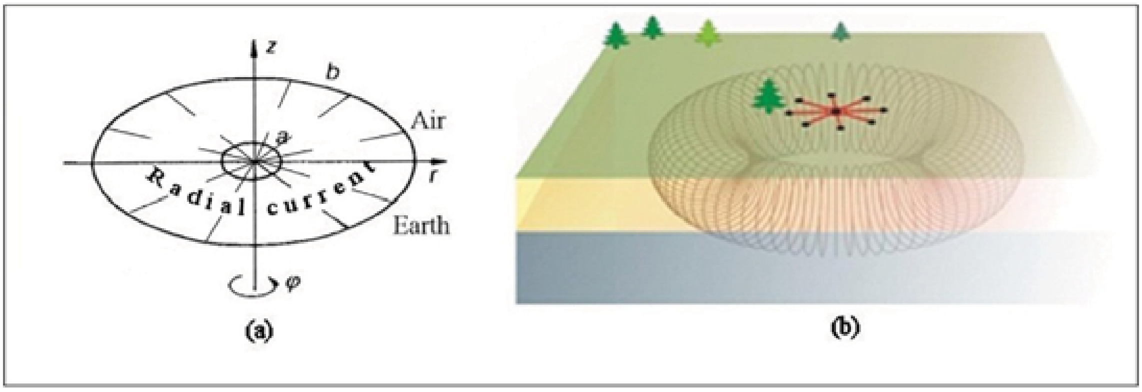

Fig. 2. The "ideal" (a) and the "real" (b) circular electric dipoles comprising two concentric electrode systems continuously and discretely distributed along the circles of radius a (central electrode) and b (outer electrode(s)), respectively. (b) Panel also schematically shows the toroidal current system induced in the earth by CED.

undoubtedly crucial in the hard-to-reach Arctic Ocean, are beyond the scope of the article. All these important issues strongly depend on the required signal-to-noise ratio.

3. Forward modeling

Although the CED method was developed almost two decades ago, and a lot of measurements were carried, no intensive modeling was carried out until very recently. This is mainly due to the fact that the method was used solely in the fixed transmitter zero magnetic field mapping mode. In the mode, only 3-D modeling is feasible, and the latter has become available for the CED method relatively recently. As for the moving short offset CED system is concerned, previous calculations have been carried out for the marine bottom located CED-*Er* array only (Goldman et al., 2015; Haroon et al., 2014). Therefore below we shall consider surface arrays, which are relevant to the proposed ice-borne CED method, and compare the responses with those of the bottom arrays. The models considered in this paper do not include the ice layer itself, as calculations for even greatly exaggerated thickness of the ice (10 m instead of the real 3–4 m) show a negligible difference in signals.

The first model is the canonical model of the marine hydrocarbon exploration (Fig. 4a), similar to the models studied for conventional CSEM investigations (e.g. Constable and Srnka, 2007). The reason for using such similar models is based on the expected similar resistivities for the ocean water, for the seawater saturated sub-seafloor medium and for the target hydrocarbon reservoir. The depth of the Arctic Ocean is known (up to 4 km deep, e.g. Weber, 1983), and it is roughly similar to the average depth of other oceans, while the depth to the expected target is selected as some average depth encountered in the previous offshore surveys.

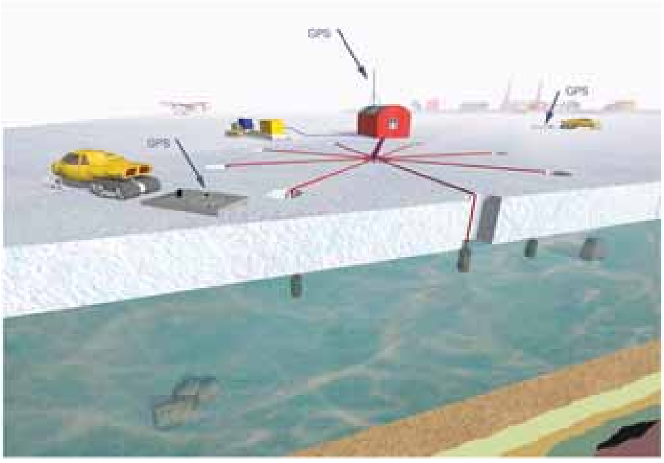

Fig. 3. Schematic layout diagram of the ice-borne CED system on a drifting ice floe. The electrodes are rigidly attached to the ice bottom for better stability.

The second model is similar to the first one, but is further complicated by the appearance of an additional 3-D object representing either another target or geologic noise. This model has been selected to study lateral resolution of the proposed method.

A current in the transmitter flows for 40 s. The responses are studied after the current is turned off. In the plots presented below, the time t = 0 corresponds to the time instant of current turning-off.

3.1. Mathematical models for electromagnetic fields calculation

To calculate the 3-D electromagnetic field induced by the CED with the radius R_{CED}, we use the vector finite element method with edge basis functions on the 3-D hexagonal unstructured mesh with terminal nodes (Persova et al., 2011). The summary (total) electric field $\vec{E}$ appears as $\vec{E} = \vec{E}^n + \vec{E}^a$, where $\vec{E}^n$ denotes the electric field of the CED in a 1-D background medium (normal field), $\vec{E}^a$ is a 3-D anomalous electric field determined by the impact of 3-D inhomogeneities. The 3-D anomalous electric field is sought from the solution of the following equation:

$$\nabla \times \frac{1}{\mu}\left(\nabla \times \vec{A}^a\right) + \sigma \frac{\partial \vec{A}^a}{\partial t} = (\sigma - \sigma^n)\vec{E}^n, \tag{1}$$

where $\vec{A}^a$ is the vector potential of the anomalous field, μ denotes the magnetic permeability, σ denotes the conductivity, σ^n denotes the conductivity in a 1-D background medium; the intensity of the anomalous electric field $\vec{E}^a$ is defined by the relation $\vec{E}^a = -\frac{\partial \vec{A}^a}{\partial t}$.

The equivalent variational formulation takes the form

$$\int_\Omega \frac{1}{\mu}\left(\nabla \times \vec{A}^a\right) \cdot \left(\nabla \times \vec{\Psi}\right) d\Omega + \int_\Omega \sigma \frac{\partial \vec{A}^a}{\partial t} \cdot \vec{\Psi} d\Omega = \int_\Omega (\sigma - \sigma^n)\vec{E}^n \cdot \vec{\Psi} d\Omega, \tag{2}$$

where the vector function $\vec{\Psi}$ is a test function, Ω is the computational domain.

The solution $\vec{A}^a$ is expressed as

$$\vec{A}^a = \sum_{i=1}^{n} q_i^a \vec{\psi}_i, \tag{3}$$

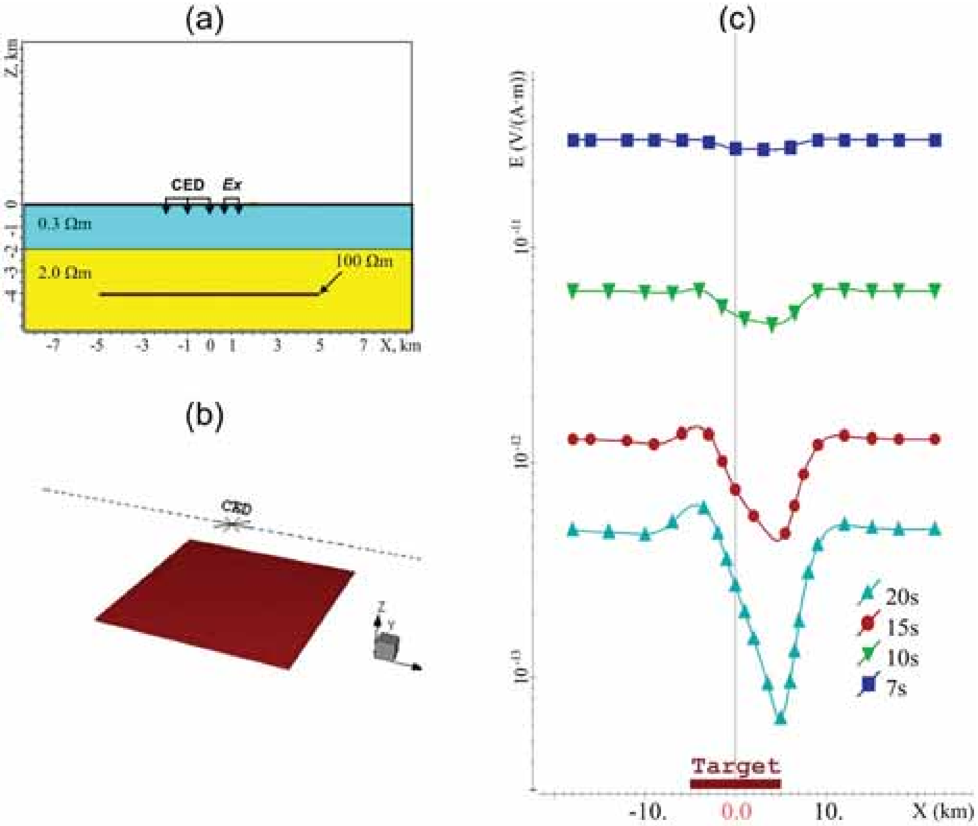

Fig. 4. Simplified 3-D geoelectric model of a hydrocarbon reservoir in the sub-seafloor sediments. (a) Cross-section; (b) 3-D view; (c) profiling responses (moving (Tx-Rx array)) at different delay times, the abscissa of the responses corresponds to the Rx center. The target is represented by a 100 m thick, 10 × 10 km^2 parallelepiped. The CED radius is 1 km, and the offset from the center is 2 km. The profile runs above the center of the target.

where $\overrightarrow{\boldsymbol{\psi}}_i$ are the basis vector functions (edge-functions), n is their number (which is precisely the number of edges in a 3-D finite element mesh).

When we substitute Eq. (3) to Eq. (2) and replace the test function $\overrightarrow{\boldsymbol{\Psi}}$ in Eq. (2) with the basis functions $\overrightarrow{\boldsymbol{\psi}}_i$ in turn, we obtain the system of linear equations

$$\boldsymbol{G}\boldsymbol{q}^a + \boldsymbol{M}\frac{\partial \boldsymbol{q}^a}{\partial t} = \boldsymbol{f},$$

where $\boldsymbol{G}$ and $\boldsymbol{M}$ are the matrixes, $\boldsymbol{f}$ is the right hand side vector. Their components are defined by the relations

$$G_{ij} = \int_\Omega \frac{1}{\mu}\left(\nabla \times \overrightarrow{\boldsymbol{\psi}}_i\right) \cdot \left(\nabla \times \overrightarrow{\boldsymbol{\psi}}_j\right) d\Omega, \ M_{ij} = \int_\Omega \sigma \overrightarrow{\boldsymbol{\psi}}_i \cdot \overrightarrow{\boldsymbol{\psi}}_j d\Omega, \tag{4}$$

$$f_i = \int_\Omega (\sigma - \sigma^n)\overrightarrow{\boldsymbol{E}}^n \cdot \overrightarrow{\boldsymbol{\psi}}_i d\Omega.$$

The $\overrightarrow{\boldsymbol{E}}^n$ field is represented as a linear combination of the basis functions $\overrightarrow{\boldsymbol{\psi}}_i$

$$\overrightarrow{\boldsymbol{E}}^n = \sum_{i=1}^{n} q_i^{en} \overrightarrow{\boldsymbol{\psi}}_i,$$

where the weights q_i^{en} are the $\overrightarrow{\boldsymbol{E}}^n$ tangential component values at the edges of the mesh. In this case the right hand side vector appears as $\boldsymbol{f} = \overline{\boldsymbol{M}}\boldsymbol{q}^{en}$, where $\overline{\boldsymbol{M}}$ is the matrix with the components $\overline{M}_{ij} = \int_\Omega (\sigma - \sigma^n)\overrightarrow{\boldsymbol{\psi}}_i \cdot \overrightarrow{\boldsymbol{\psi}}_j d\Omega$.

The time discretization of $\frac{\partial \boldsymbol{q}^a}{\partial t}$ is performed with the use of the three-step implicit scheme (Persova et al., 2011).

The normal field (the CED field in a horizontally-layered medium) is fully described by the only non-zero component of the magnetic field $H_\varphi(r,z,t)$ that is sought as the equation solution

$$-\nabla \cdot \left(\frac{1}{\sigma^n}\nabla H_\varphi\right) + \frac{1}{\sigma^n r^2}H_\varphi + \mu\frac{\partial H_\varphi}{\partial t} = 0, \ [H_\varphi]|_{\Gamma_{\text{CED}}} = \frac{I(t)}{2\pi r}, \tag{5}$$

where Γ_{CED} is the horizontal surface on which the ideal CED is located (i.e. Γ_{CED} is the circle with the radius R_{CED}), $[H_\varphi]$ is the H_φ jump on Γ_{CED}, $I(t)$ is the current value in the CED. The boundary condition $H_\varphi = 0$ is set on the border between the conductive medium and air. If the CED is located on the border between the conductive medium and air, then, instead of the H_φ jump on Γ_{CED}, the boundary condition $H_\varphi|_{\Gamma_{\text{CED}}} = \frac{I(t)}{2\pi r}$ is set.

The values of the $\overrightarrow{\boldsymbol{E}}^n$ field can be calculated as follows. At first, with the use of H_φ values, the fields $E_r(r,z,t)$ and $E_z(r,z,t)$ are calculated in the cylindrical coordinate system

$$E_r = -\frac{1}{\sigma}\frac{\partial H_\varphi}{\partial z}, E_z = \frac{1}{\sigma}\left(\frac{\partial H_\varphi}{\partial r} + \frac{H_\varphi}{r}\right). \tag{6}$$

The values of the $\overrightarrow{\boldsymbol{E}}^{n}$ field in the Cartesian coordinate system can be calculated by the following formulae:

$$E_x(x,y,z,t) = E_r\left(\sqrt{(x-x_0)^2+(y-y_0)^2}, z, t\right)\frac{x-x_0}{\sqrt{(x-x_0)^2+(y-y_0)^2}},$$

$$E_y(x,y,z,t) = E_r\left(\sqrt{(x-x_0)^2+(y-y_0)^2}, z, t\right)\frac{y-y_0}{\sqrt{(x-x_0)^2+(y-y_0)^2}},$$

$$E_z(x,y,z,t) = E_z\left(\sqrt{(x-x_0)^2+(y-y_0)^2}, z, t\right),$$

where x_0, y_0 are coordinates of the CED center.

The equivalent variational formulation for the normal field takes the form

$$\int_{\Omega^c}\frac{1}{\sigma^n}\nabla H_\varphi \nabla v d\Omega + \int_{\Omega^c}\frac{1}{\sigma^n r^2}H_\varphi v d\Omega + \int_{\Omega^c}\mu\frac{\partial H_\varphi}{\partial t}v d\Omega = 0,\ [H_\varphi]\big|_{\Gamma_{\text{CED}}} = \frac{I(t)}{2\pi r}, \tag{7}$$

where the function $v(r,z)$ is the test function, Ω^c is the computational domain in the cylindrical coordinate system.

The solution H_φ is expressed as

$$H_\varphi = \sum_{i=1}^{n^c} q_i^H \psi_i, \tag{8}$$

where $\psi_i(r,z)$ are the node basis functions, n^c is their number (which is precisely the number of nodes in a 2-D finite element mesh).

When we substitute Eq. (8) to Eq. (7) and replace the test function v in Eq. (7) with the basis functions ψ_i in turn, we obtain the system of linear equations

$$\boldsymbol{G}^c\boldsymbol{q}^H + \boldsymbol{M}^c\frac{\partial \boldsymbol{q}^H}{\partial t} = \boldsymbol{f}^c,$$

where $\boldsymbol{G}^c$ and $\boldsymbol{M}^c$ are the matrixes the components of which are calculated as

$$G_{ij}^c = \left(\int_{\Omega^c}\frac{1}{\sigma^n}\nabla\psi_i\nabla\psi_j r\mathrm{d}r\mathrm{d}z + \int_{\Omega^c}\frac{1}{\sigma^n}\frac{1}{r}\psi_i\psi_j\mathrm{d}r\mathrm{d}z\right),\quad M_{ij}^c = \int_{\Omega}\mu\psi_i\psi_j r\mathrm{d}r\mathrm{d}z.$$

The components of the right hand side vector are calculated as

$$f_i = \frac{I(t)}{2\pi}\sum_{j\in N}\left(\int_{\cup\Omega_m^c}\frac{1}{\sigma^n}\nabla\psi_i\nabla\psi_j\mathrm{d}r\mathrm{d}z + \int_{\cup\Omega_m^c}\frac{1}{\sigma^n}\frac{1}{r^2}\psi_i\psi_j\mathrm{d}r\mathrm{d}z\right) + $$
$$+\frac{1}{2\pi}\frac{\partial I(t)}{\partial t}\sum_{j\in N}\left(\int_{\cup\Omega_m^c}\mu\psi_i\psi_j\mathrm{d}r\mathrm{d}z\right),$$

where Ω_m^c are the finite elements the upper border of which lies on Γ_{CED}.

The time discretization of $\frac{\partial \boldsymbol{q}^H}{\partial t}$ is performed with the use of the three-step implicit scheme (Persova et al., 2011).

3.2. 3-D single target model

Fig. 4 shows the model (left) and the profiling data at different measurement times (right). This plot (and the plots given below, except Fig. 5b) shows the normalized electric field per Amp of the current in CED. The current in CED is defined as a sum of currents in eight wires (suppose the current in each wire is 500 A, then the current in CED is 4000 A). One can see that the target is clearly detected starting from roughly 10 s (i.e. 10 s after the current is turned off). With increasing the measurement time, the edge effect significantly increases but on the account of a smaller signal.

Previously, the modeling was performed for the bottom located CED array in Goldman et al. (2015). That modeling was carried out using a modified spectral Lanczos decomposition method by Druskin and Knizhnerman (1988). In Goldman et al. (2015) the dimensions of the array were significantly smaller: the CED radius was 100 m, and the offset was 200 m. Using the approach presented here (Section 3.1) we have repeated those calculations for one of the geoelectrical models presented in Goldman et al. (2015) and shown in Fig. 5a. These calculation results are shown in Fig. 5b (this plot presents the signal normalized by the current in the wire as in Goldman et al. (2015)). They are in good agreement with the results presented in Goldman et al. (2015). As seen from Fig. 5b, the profiling response consists of two roughly equal anomalies of different polarity strictly above the edges of the target.

For the geoelectrical model and CED array dimensions (CED radius and offsets) considered in this paper (Fig. 4), the behavior of profiling response (for each time instant) from the target is somewhat different (Fig. 4c), i.e. the profiling response is unimodal and asymmetrical.

Further analysis shows that such different behaviors are not caused by the difference in the location of the arrays (surface or bottom), but rather by significantly different dimensions of the arrays. Goldman et al. (2015) considered very short, practically point arrays, and, as a result, the profiling responses above the target were rather symmetrical.

As for the signal detectability is concerned, the difference between the surface and bottom located CED systems is also insignificant. Indeed, Fig. 6 shows the total and background transient responses above the

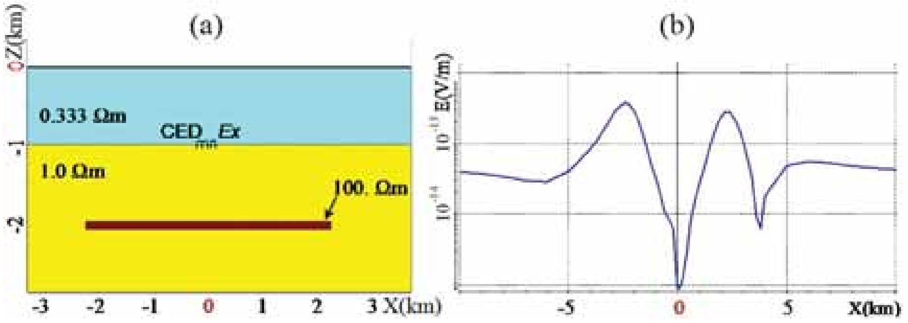

Fig. 5. Geoelectric model of a hydrocarbon reservoir and the bottom CED system considered in (Goldman et al., 2015). The target is represented by a 100 m thick, 4.5 × 4.5 km^2 parallelepiped. The CED radius is 100 m, and the offset from the center is 200 m. (a) Cross-section; (b) profiling responses (moving (Tx-Rx array)) at time instant of 10 s.

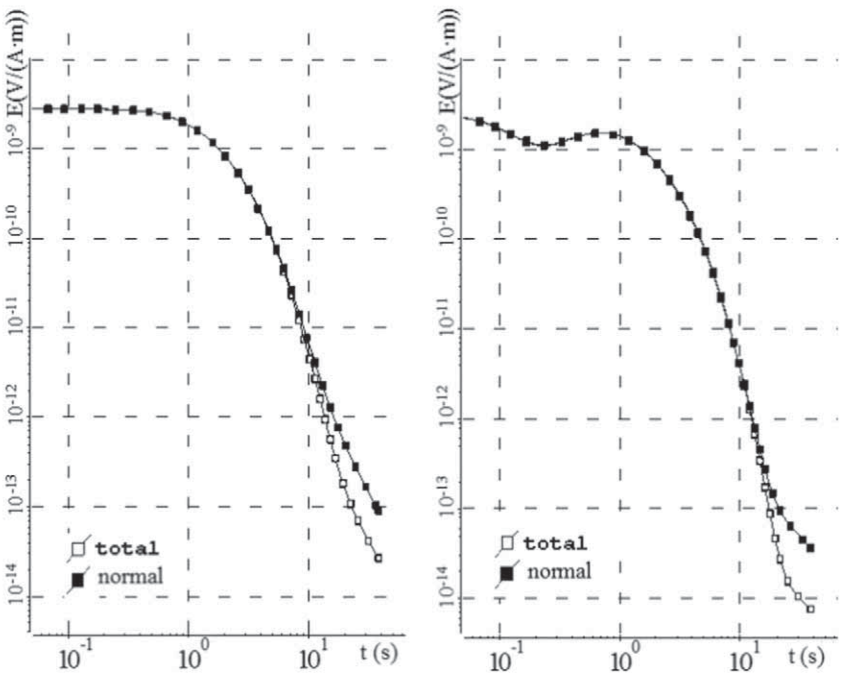

Fig. 6. CED transient responses for the model shown in Fig. 4a. The responses for the surface array are shown in the left, the responses for the bottom array are shown in the right. CED is located above the middle of the target. The CED radius is 1 km, and the offset from the center is 2 km. "Total" stands for the response including target; "normal" stands for the background response.

center of the target for both the surface (left) and bottom (right) located CED transmitters. The detectability of the bottom array is somewhat higher than that of the surface array, but the total signal and, as a result, the exploration depth are significantly lower at the same measurement time. Therefore, practically, it is more preferable to use the stable surface CED system with the electrodes rigidly attached to the bottom of the ice.

The proposed system utilizes short offset arrays and, as such it is expected to demonstrate significantly higher lateral resolution than that of long offset methods (CSEM, LOTEM). To verify this, we shall start with the simplest case of a single target with variable lateral dimensions. Fig. 7 shows profiling responses for different target dimensions at time 20 s. The choice of such late time is dictated by visual considerations only. In reality, this time should be selected as a compromise between the required lateral resolution and the existing signal-to-noise ratio (SNR). For instance, if the expected size of the target in the model under consideration is less than roughly 3 × 3 km, the system must provide the sufficient SNR up to 20 s. If the target is roughly three times larger, the required measurement time can be reduced to some 10 s, and the signal will increase by approximately two orders of magnitude (compare Figs. 4 and 7). It is important to emphasize that, contrary to conventional long offset methods (LOTEM, CSEM, etc.), the lateral resolution of the proposed system is mainly limited by the SNR rather than by inherent signal detectability. Of course, there is some minimum threshold size of the target, below which it cannot be detected due to the limited signal detectability. But this scenario takes place for much smaller sizes of the target than those considered above (Goldman et al., 2015). It is important to underline that lateral resolution in CED manifests itself not only in high target responses from relatively small objects, but also in the shape of profiling responses at sufficiently late times. The appearance of sharp extremes exactly above the edges of the target (Figs. 4 and 7) might aid in initial visualization of the data acquired and selection of those segments of the traverse, where further multidimensional inversion should be performed.

In many cases, we not only need to detect relatively small targets, but also to distinguish between adjacent subsurface features. This problem is much more complicated than the above considered detectability so that a simple visualization might be insufficient to solve it. In order to obtain quantitative information about the object(s), we propose applying the specially designed multidimensional inversion (Persova et al., 2013) to those segments of the CED profile, where the object has been detected.

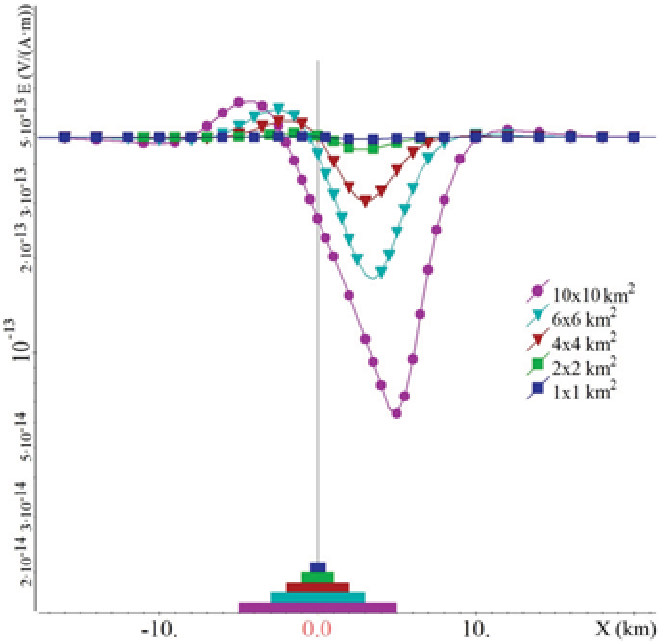

Fig. 7. CED profiling responses for the model shown in Fig. 4a with variable target dimensions. Each response corresponds to the appropriate target shown in the bottom with the same color.

4. Inversion

The inversion is based on the assumption that the geoelectric parameters of the 1-D background model are known and can be fixed during the inversion. Such an assumption is well justified in the marine environment where the resistivity of sea water and to some extent of sea water saturated sediments is well known as well as the thickness of the upper layer representing the bathymetry. The variable parameters of the inversion are resistivities and geometrical parameters of 3-D objects, which are represented by parallelepipeds of different dimensions at different depths.

4.1. Multidimensional inversion algorithm

The parameters of a three-dimensional geoelectrical model will be determined on the basis of the functional minimization

$$\Phi(\boldsymbol{b}) = \sum_{l=1}^{L}\sum_{k=1}^{K}\left(v_{lk}\delta\varepsilon_{lk}(\boldsymbol{b})\right)^2 + \sum_{m=1}^{M}\alpha_m(\Delta b_m)^2, \tag{9}$$

where the first term is an error (or residual), and the second one is a regularizing additive.

The notation in formula (9) is the following. $\delta\varepsilon_{lk} = \tilde{\varepsilon}_{lk} - \varepsilon_{lk}$ are the errors (residuals) in the signals, ε_{lk} is the signal measured in the l-th receiver at time t_k, $\tilde{\varepsilon}_{lk}$ are the corresponding theoretical signals obtained by solving the forward three-dimensional problem, $\boldsymbol{b}$ is a vector of the unknown parameters b_m, $\boldsymbol{b}^0$ is a vector of parameters b_m^0 obtained from the previous iteration of the nonlinear inversion, $\Delta b_m = b_m - b_m^0$, α_m are the regularization parameters, v_{lk} are some weights defined by the level of noise in the l-th receiver and the scale of time changing of the signal received. The vector of the desired parameters $\boldsymbol{b}$ includes conductivity values of the required objects as well as the varying coordinates of the boundaries of these objects. On doing inversions described in the Sections 4.3 and 4.4, we used the following parameterization of the geoelectrical model. As the characteristics of two objects were being recovered, 2 values of conductivity and 12 geometrical parameters were taken as the parameters b_m in 3-D inversion. The geometrical parameters were the following: two x-coordinates, two y-coordinates, and two z-coordinates for each of the two recovered objects. Consequently, in 2-D inversion 2 values of conductivity and 8 geometrical parameters were taken as the parameters b_m.

The minimization of functional (9) is based on the linearization of theoretical signals $\tilde{\varepsilon}_{lk}$ by the parameters b_m in the neighborhood of b_m^0. As a result, the difference $\delta\varepsilon_{lk}$ between the theoretical $\tilde{\varepsilon}_{lk}$ and measured ε_{lk} signals are represented as

$$\delta\varepsilon_{lk}(\boldsymbol{b}) \approx \delta\varepsilon_{lk}\left(\boldsymbol{b}^0\right) + \sum_{m=1}^{M}\frac{\partial(\delta\varepsilon_{lk})}{\partial b_m}\Delta b_m, \tag{10}$$

where $\frac{\partial(\delta\varepsilon_{lk})}{\partial b_m}$ are the derivatives reflecting the impact of the m-th parameter change in the l-th receiver at time instant t_k.

As a result, the minimized functional (9) takes the form

$$\tilde{\Phi}(\boldsymbol{b}) = \sum_{l=1}^{L}\sum_{k=1}^{K}\left(v_{lk}\delta\varepsilon_{lk}\left(\boldsymbol{b}^0\right) + v_{lk}\sum_{m=1}^{M}\frac{\partial(\delta\varepsilon_{lk})}{\partial b_m}\Delta b_m\right)^2 + \sum_{m=1}^{M}\alpha_m(\Delta b_m)^2. \tag{11}$$

For calculating the fields of 3-D objects impacts while determining the values $\frac{\partial(\delta\varepsilon_{lk})}{\partial b_m} \approx \frac{\Delta(\varepsilon_{lk})}{\Delta b_m^e}$ in the functional (11) the following mathematical model is used

$$\nabla\times\left(\frac{1}{\mu_0}\nabla\times\ \vec{\boldsymbol{A}}^a\right) + \sigma\frac{\partial\vec{\boldsymbol{A}}^a}{\partial t} = \left(\sigma - \sigma^{3D\_0}\right)\vec{\boldsymbol{E}}^{3D\_0}, \tag{12}$$

where σ^{3D_0} and $\vec{\boldsymbol{E}}^{3D\_0}$ are the distributions of conductivity and intensity of the electric field in the 3-D medium for which the field was calculated at the previous iteration of nonlinear inversion, σ is the conductivity of the medium obtained by adding the reference increment Δb_m^e to the parameter b_m^0.

As a result of minimizing the functional (11) in Δb_m, we obtain the following system of linear equations

$$(\boldsymbol{C} + \boldsymbol{\alpha})\Delta\boldsymbol{b} = \boldsymbol{d}, \tag{13}$$

where $\boldsymbol{\alpha}$ is the diagonal matrix with the components α_m on the main diagonal. The elements of the matrix $\boldsymbol{C}$ and the right hand side vector $\boldsymbol{d}$ are determined by the relations

$$C_{ij} = \sum_{l=1}^{L}\sum_{k=1}^{K}(\nu_{lk})^2\frac{\partial(\delta\varepsilon_{lk})}{\partial b_i}\frac{\partial(\delta\varepsilon_{lk})}{\partial b_j},$$

$$d_i = -\sum_{l=1}^{L}\sum_{k=1}^{K}(\nu_{lk})^2\delta\varepsilon_{lk}\left(\boldsymbol{b}^0\right)\frac{\partial(\delta\varepsilon_{lk})}{\partial b_i},\quad i,j = 1\ldots M.$$

The geometrical parameterization used for recovering the geoelectrical model allows the adaptive choice of regularization parameters and thereby improving the nonlinear inversion convergence.

The regularization parameters α_m at each iteration of nonlinear inversion are determined as follows. First, we prescribe some (rather small) initial values α_m (they are scaled properly for geometrical parameters and conductivities), and the values of increments Δb_m are calculated by solving the system (13).

Then, it is checked that each of the values $b_m = b_m^0 + \Delta b_m$ stay within the bounds set for the m-th parameter. Besides, for geometrical parameters, it is checked that the values of the coordinates of the left (bottom) borders of an object do not exceed the values of the coordinates of the right (upper) borders of an object and do not excessively approach them. It is also checked that the borders of each recovered object do not intersect other objects. For parameters b_m for which this condition is violated, the corresponding regularization parameters increase χ times (we use $\chi = 2$), and the solution of system (13) is repeated. As the order of the system (13) is very small, this procedure requires very low computational cost, but makes it possible to obtain new parameters b_m which both minimize the linearized functional $\tilde{\Phi}(\boldsymbol{b})$ and satisfy the constrains imposed to b_m. As a result, the convergence of the nonlinear inversion is significantly improved.

4.2. 3-D multiple objects model

We consider as an example a simplified model consisting of two objects located at the same depth but at different distances from each other (Fig. 8). Fig. 9 shows the profiling responses for the case, when the objects are visually separated (left) and the case, when the profiling response looks as slightly distorted single body response (right). In the former case, we can efficiently apply the abovementioned inversion algorithm and not only qualitatively separate the objects, but also to obtain a quantitative information regarding the resistivities and the geometrical parameters of both bodies. We now consider three scenarios:

1. The profile runs above the center of the objects and the 2-D inversion algorithm is applied. The data for one offset along the profile, as shown in Fig. 10a, are used in the inversion.
2. The profile runs above the center of the objects and the 3-D inversion algorithm is applied. For greater stability of the inversion, the data for twenty symmetrical offsets, as shown in Fig. 10b, are used in the inversion.
3. The centers of the objects are shifted from the profile as shown in Fig. 10c and the 3-D inversion algorithm is applied. Again,

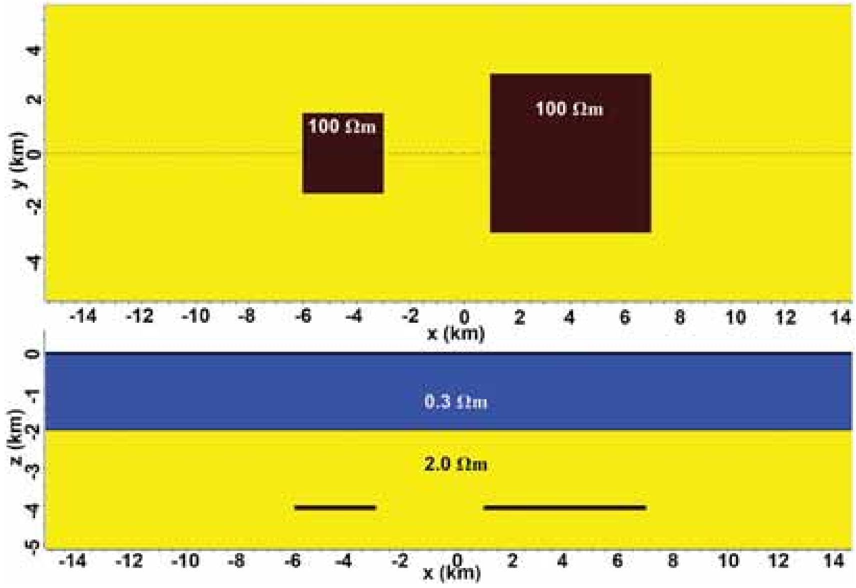

Fig. 8. Simplified model of multiple 3-D objects located at the same depth. The upper panel represents the plane view; the lower panel represents the cross-section. This model is used for generating the data for further inversion. During the inversions the parameters of the background medium are fixed, while all the parameters of both objects are variable.

the data for twenty symmetrical offsets (see Fig. 10c), are used in the inversion.

4.3. 2-D inversion

To select the initial model, we fix background parameters and estimate the number of objects from the profiling response. The minimum number of objects for the model in question (Fig. 8) is determined as two from Fig. 9 (left). The initial and final models as well as the forward responses for two measurement times are shown in Fig. 11a and b, respectively. The inversion has converged after 23 iterations with a total RMS error for all the times and receivers of 0.9%. Comparison of the inverted and "true" models (Figs. 8 and 11b) shows that the lateral geometric parameters of both objects are recovered fairly accurately, the resistivity and the depths are underestimated and the thicknesses are slightly overestimated, particularly that of the larger object. It should be noted that considering 1-D background model is not justified e.g. under sharp bathymetrical conditions. In this case, the inversion algorithms discussed above should be modified to account for the seafloor relief. Nevertheless, for the theoretical investigation of a lateral resolution, the abovementioned simplified inversion scheme seems well justified.

4.4. 3-D inversion

The initial model used for the 3-D inversions is almost identical to that used in the 2-D inversion (Fig. 11a). The only difference is that both objects have final dimensions in the y-direction equal to those in the x-direction. The inversion along the central profile (Fig. 12, left) revealed the model quite similar to the "true" model (compare Figs. 12,

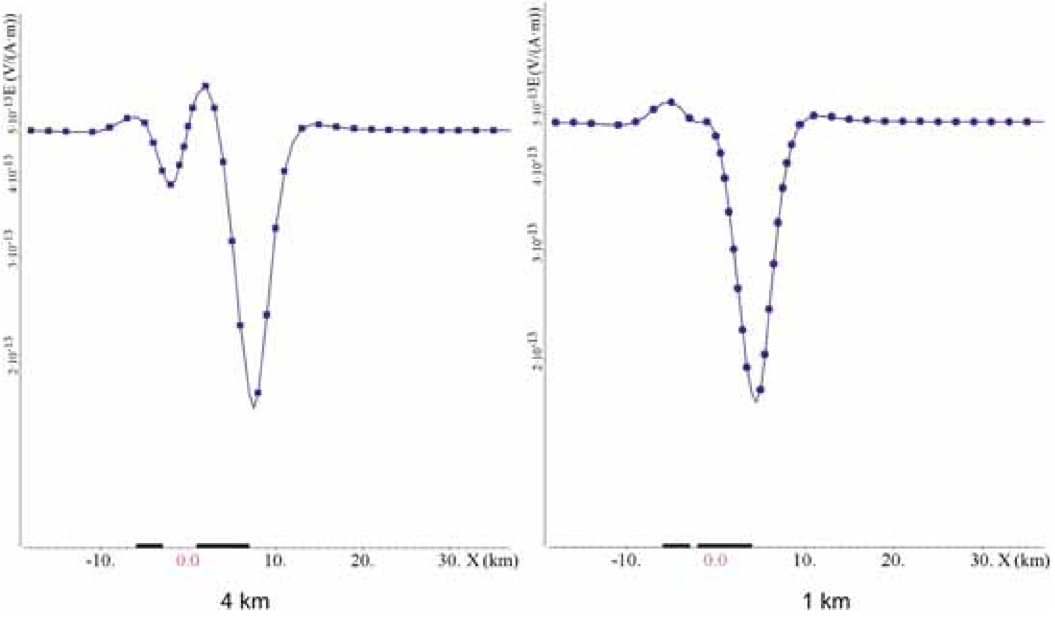

Fig. 9. Profiling responses above two 3-D objects. Left: the distance between the objects is 4 km (clearly resolved); right: the distance between the objects is 1 km (visually unresolved in presence of noise).

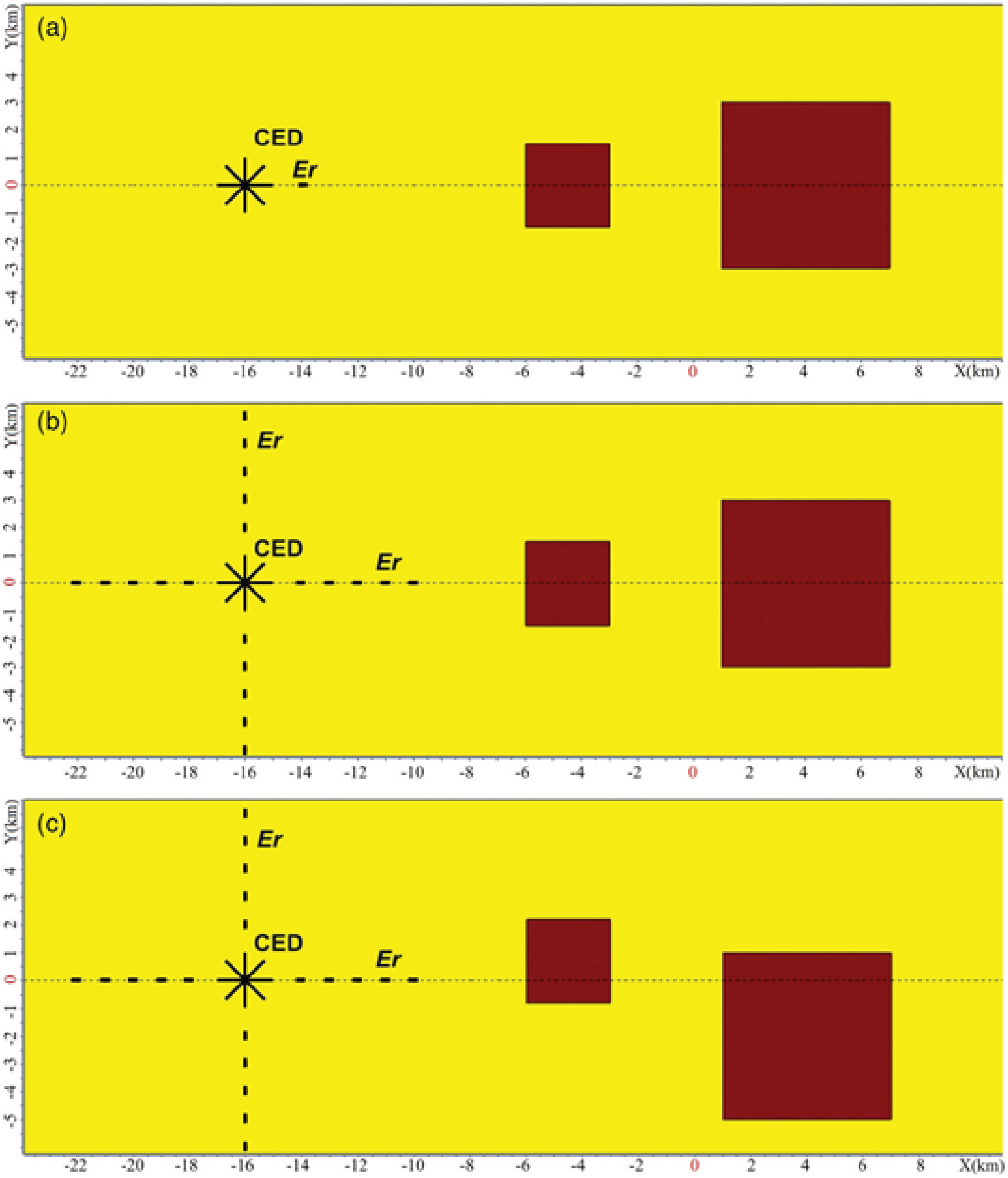

Fig. 10. CED arrays used in the inversion. (a) 2-D inversion along the central profile; (b) 3-D inversion along the central profile; (c) 3-D inversion for the objects shifted from the profile.

left and 8). The only difference is in somewhat lower resistivities and prolonged dimensions in the y-direction. The inversion with the shifted objects led to better estimated dimensions of the larger object, but to somewhat underestimated depth.

Since all three inversions are based on significantly oversimplified models, the abovementioned small differences in the results cannot be used for real practical recommendations. The main practically important result is that the proposed 2-D inversion of essentially 3-D data does not lead to unacceptable errors, and thus the significantly simpler 2-D field acquisition set up can be used in the ice-borne CED measurements. It is particularly important because of a rather limited size of ice floes in summer time (less than a few kilometers in either direction) that might prevent utilizing large arrays necessary for the 3-D acquisition (Fig. 10b, c)

It should be noted that inverting these synthetic data, which are generated using simple model geometry, gives only very preliminary idea regarding the ability of the proposed inversion to interpret real data. However, even these preliminary results suggest that under the specific conditions considered (homogeneous background with some known geoelectric parameters), the proposed inversion algorithm may be usable in quantitative evaluating parameters of relatively simple exploration targets.

5. Distortions of the CED system

All the above analysis was based on assuming ideally symmetrical CED both geometrically and regarding the currents in individual legs. Although geometrical errors and current instability are typical for all GE/GEM methods, they might be crucial in CED and VED methods because of the quasi-exponential smallness of the signal at late times in presence of resistive structures (Goldman et al., 2015). For example, in case of VED, even slight non-verticality produces parasitic horizontal electric components, which decay much slower in time and thus might produce significant errors sometimes exceeding the desired target response. Fortunately, in case of CED, non-horizontality is not an issue (Haroon et al., 2014), but asymmetrical positions of electrodes and/or current lines as well as inequality of currents within individual CED legs might lead to significant errors in the measured signal.

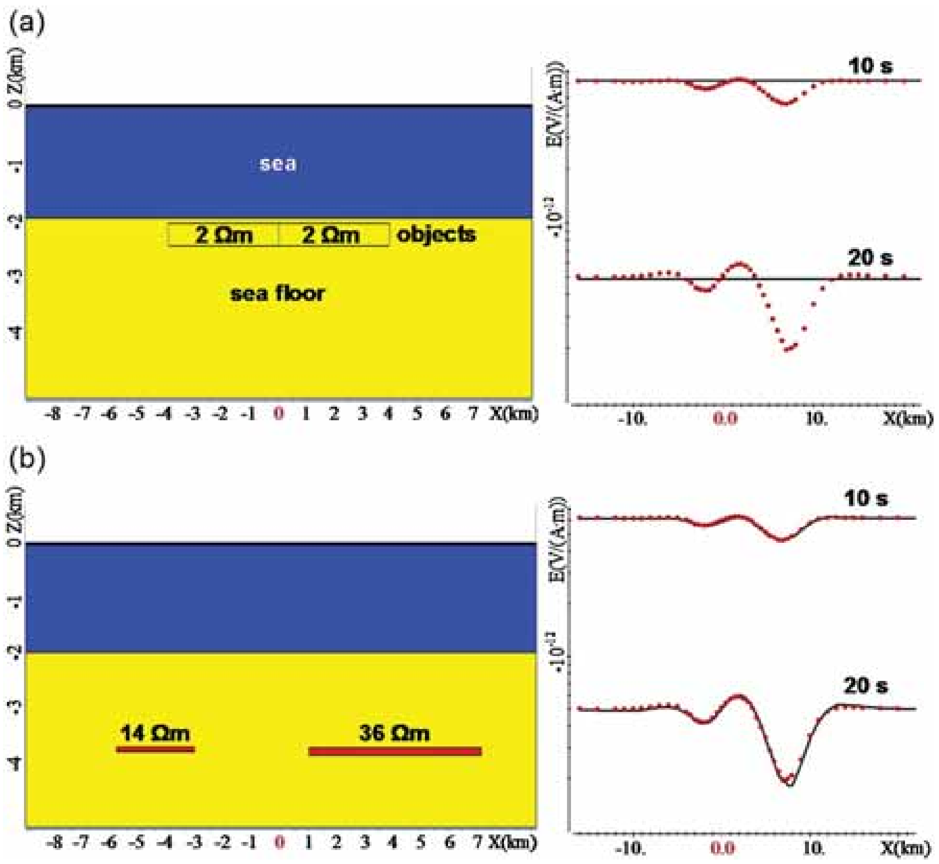

Fig. 11. 2-D inversion of synthetic data generated using 3-D model in Fig. 8. (a) Initial model; (b) final model. The curves in the right represent the generated 3-D data (red points) and forward responses for the model in the left (solid curves) at two measurement times of 10 s and 20 s.

Fig. 13 demonstrates the influence of three main distortions expected in the proposed ice-borne CED system. The calculations are carried out for the canonical background model (Fig. 4a) using CED of 1 km radius and 2 km offset from the CED center. Fig. 13(a) and (d) demonstrates the influence of the improper geometry of the current lines, while the electrodes are located in right positions. This is the realistic scenario since the electrodes can be fixed fairly accurate using differential GPS, while laying down perfectly symmetrical long cables is technically very difficult. One can see from the figures that the asymmetry up to 60 m does not produce significant errors in the measured signal (less than 15%) in the whole time range considered and less than 5% for t < 10 s.

Fig. 13(b) and (e) shows the influence of the current inequality (in per cents of the current in a “distorted” electrode compared to “undistorted” currents). Contrary to the geometry of current lines, this distortion sharply increases with time and for the 0.6% error might

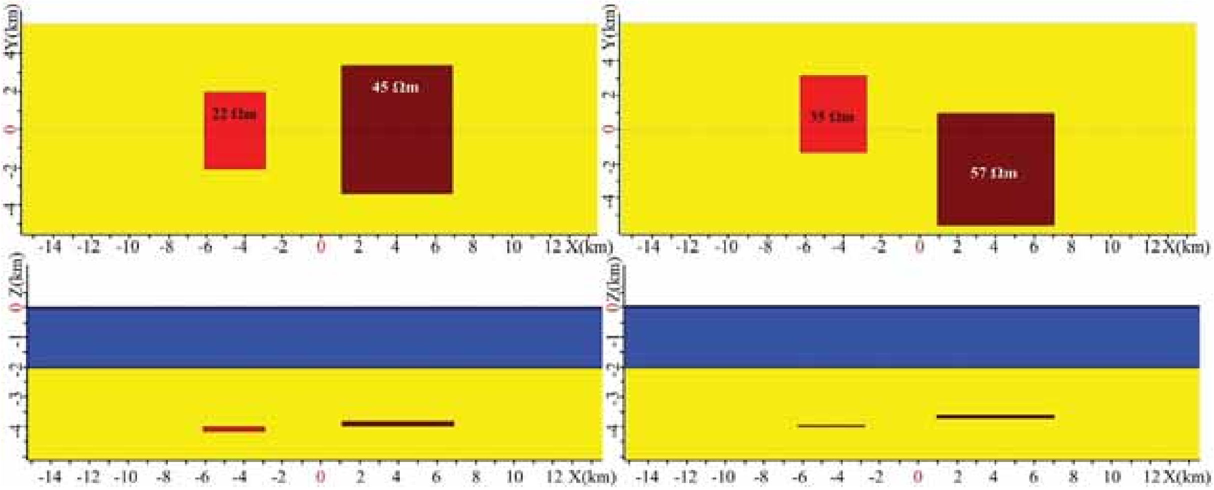

Fig. 12. 3-D inversion of synthetic data generated using 3-D model in Fig. 8. Left panel shows the final model obtained along the profile running above the center of the objects (see Fig. 10b). Right panel shows the final model obtained for the shifted objects (see Fig. 10c).

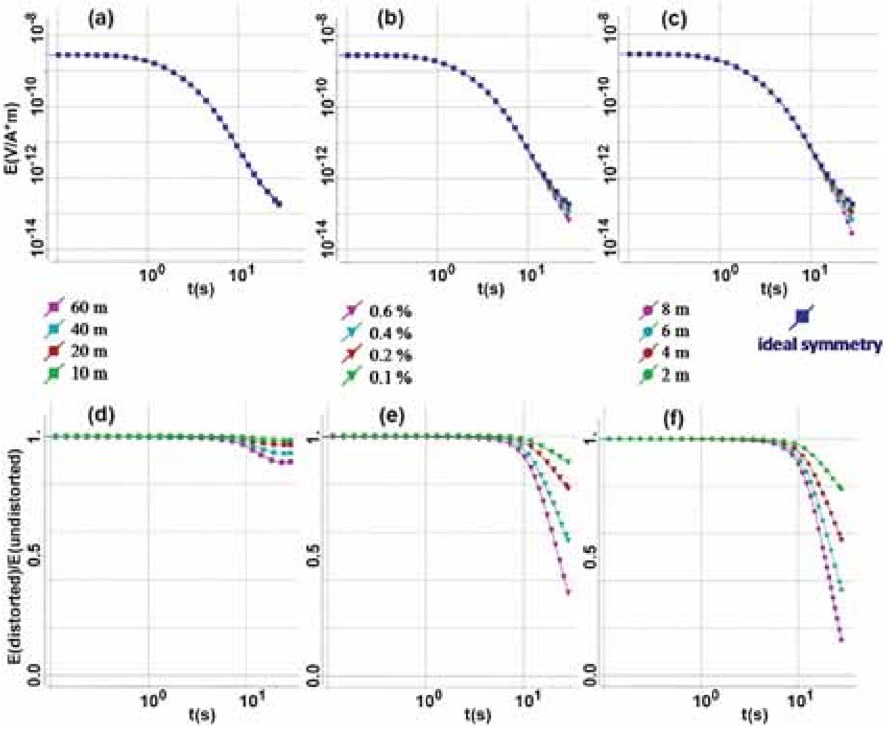

Fig. 13. The influence of the CED system distortions on the measured signals. The upper panel compares distorted and undistorted signals; the lower panel shows the ratios of the distorted signals to the undistorted one. The leftmost pictures show the distortion of the current lines, the rightmost pictures show the influence of asymmetrical electrode positions and the pictures in the middle demonstrate the influence of the current inequality.

become quite significant at times t > 20 s. Fortunately, due to the relatively high homogeneity of the ocean water (compared to that of the ground) the current instability can be easily reduced to less than 0.1% using already available current stabilizators (Mogilatov and Balashov, 1996).

Fig. 13(c) and (f) shows the influence of the electrode location. Similarly to the current instability, this influence dramatically increases with time and might become very significant at late times (t > 20 s), if the “distorted” electrode is shifted more than 5 m from its correct position. Again, using available differential GPS the electrodes can be positioned even much more accurate.

Thus, all three considered distortions are either insignificant or can be reduced to an acceptable level by means of existing methods and instruments.

6. Signal measurability and the estimate of possible noise impact

To start with, we estimate the fundamental measurability of the signal for the technology considered in this paper (further, we will call it CED/HEL technology). In doing this, we compare the signals which can be obtained for this technology with the data presented in the paper (Helwig et al., 2013) for the technology using vertical electrical dipoles/lines (VED/VEL technology). In that paper Fig. 4 presented the data measured in the Barents Sea (the Snøhvit field, at 70°N). The length of the vertical transmitter dipole was about 300 m, the current value was 6000 A. The length of the vertical receiver was 10 m. The signals (shown in Fig. 4) were given in units of V/(A·m) (i.e. normalized by current). At time instant $t = 6$ s after turning-off the current in the transmitter, the value of the signal was 4×10^{-13} V/(A·m). We conclude that the signal 2.4×10^{-8} V was successfully measured by the receiver of 10 m in length.

For the CED/HEL technology and for CED system dimensions ($R = 1000$ m) and geoelectrical model presented in the section “Forward modeling”, the value of the signal at time instant $t = 20$ s (when the values of abnormal signal are sufficient for target identification) is 6×10^{-7} V for the same current value (6000 A) and the horizontal receiver line of 1000 m in length. Thus, the signal is measurable even at marked decrease of current value in the CED.

To estimate the actual feasibility of the technology considered, it is necessary to study the possible noise impacts.

At first, we estimate what ratio between the magnetotelluric signals (MT-signals) and the useful signals may be at the instant of time when the target is detectable. Once the magnitude of MT-signals is unknown to us, we apply the following approach for estimating the possible impact of MT-noise.

For a very approximate upper estimate of possible level of MT-current, we use the data presented in the paper (Helwig et al., 2013) again. We proceed from the assumption that the maximum level of MT-signals $\varepsilon_{\mathrm{VEL}}^{\mathrm{MT}}$ (here and further the superscript denotes the source type, the subscript denotes the receiver type) does not exceed 20% of the measured useful signal $\varepsilon_{\mathrm{VEL}}^{\mathrm{VED}}$. Obviously, the MT-signals measured by the vertical receiver can be caused only by 2-D or 3-D inhomogeneities. It can be, for example, the target itself or near bottom inhomogeneities (the change of the sea depth or local changes in conductivity of near bottom layers).

To perform an upper estimate of the possible level of MT-current, we consider the geoelectrical model formed on the basis of the measurements results obtained by the VED/VEL technology and presented in the paper (Helwig et al., 2013). We include the 3-D inhomogeneity into the geoelectrical model, which corresponds to the target and induces the signals corresponding to measurements presented in the paper (Helwig et al., 2013). Moreover, we include 3-D inhomogeneities into the geoelectrical model, which corresponds to possible sea depth changes. The vertical section of this geoelectrical model is shown in Fig. 14a. The receivers' locations are shown by green points.

Fig. 14b shows the ratios of $\varepsilon_{\mathrm{VEL}}^{\mathrm{MT}}$ to $\varepsilon_{\mathrm{VEL}}^{\mathrm{VED}}$, where $\varepsilon_{\mathrm{VEL}}^{\mathrm{MT}}$ are MT-signals (further we will consider them as noises) in the vertical receivers of 10 m in length for two frequencies (0.3 Hz and 0.03 Hz) in the range corresponding to the time range of target detectability. These signals have been calculated (by means of 3-D modeling of MT-fields (Persova et al.,

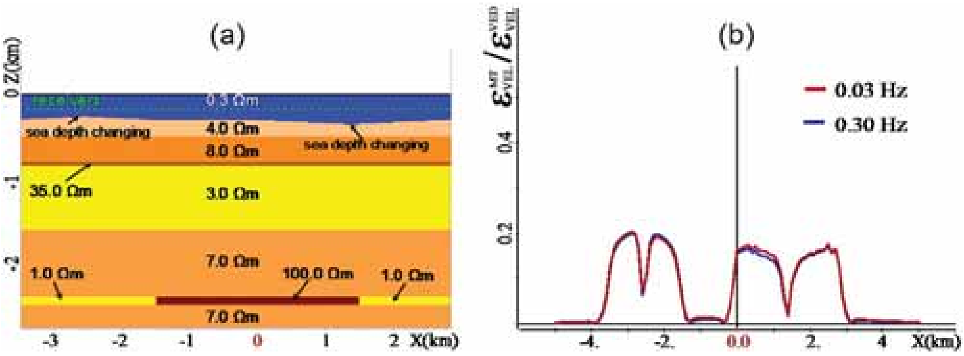

Fig. 14. (a) The cross-section of the geoelectrical model used to estimate a possible MT-noise; (b) ratios of the calculated MT-signals $\varepsilon_{\mathrm{VEL}}^{\mathrm{MT}}$ to the useful signal $\varepsilon_{\mathrm{VEL}}^{\mathrm{VED}}$ in the vertical receivers of 10 m in length for two frequencies (0.3 Hz and 0.03 Hz)

2011)) at such values of the MT magnetic field on the sea surface, which correspond to the signals with the maximum value of 4.8×10^{-9} V (i.e. 20% of 2.4×10^{-8} V) in vertical receivers. Then the calculated MT-signals have been divided into 2.4×10^{-8} V. This value corresponds to the signal $\varepsilon_{\mathrm{VEL}}^{\mathrm{VED}}$ measured by the vertical receiver at time instant $t = 6$ s (recall that this signal corresponds to the current of 6000 A in the vertical transmitter dipole and 10 m vertical receiver and is obtained by multiplying the signal presented in Fig. 4 in the paper (Helwig et al., 2013) by 60,000).

We use the same values of the MT magnetic field on the sea surface for determining the level of possible MT-noises that impact the signals (we will call these signals $\varepsilon_{\mathrm{HEL}}^{\mathrm{CED}}$) measured in the CED/HEL technology (considered in our paper). In this case we have used the geoelectrical model of a similar nature (including the depth target and near bottom inhomogeneities) shown in Fig. 15a.

In Fig. 15b the ratios of the calculated MT-signal ($\varepsilon_{\mathrm{HEL}}^{\mathrm{MT}}$) to the useful signal $\varepsilon_{\mathrm{HEL}}^{\mathrm{CED}}$ (obtained for the current 6000 A in CED) in horizontal receivers are shown (the receivers' locations are shown by green points in Fig. 15a). Obviously, the MT-noise/signal ratio in this case by comparison with the situation considered in the paper (Helwig et al., 2013) (when using the VED/VEL technology) is deteriorated approximately 100 times.

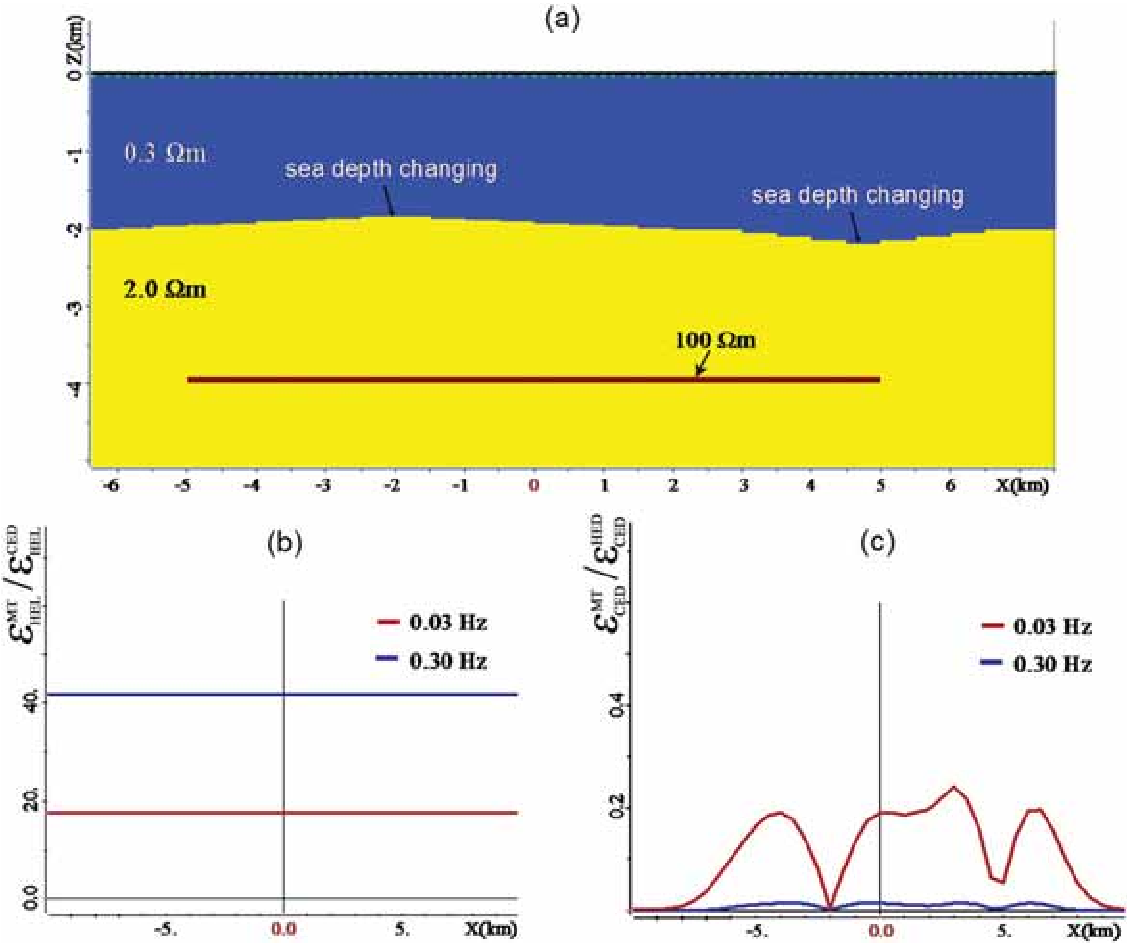

Fig. 15. (a) The cross-section of the geoelectrical model used to estimate the MT-noise/signal ratio for the CED/HEL and HED/CED technologies; (b) ratios of the calculated MT-signals $\varepsilon_{\mathrm{HEL}}^{\mathrm{MT}}$ to the useful signal $\varepsilon_{\mathrm{HEL}}^{\mathrm{CED}}$ in the horizontal receivers of 1000 m in length for two frequencies: 0.3 Hz and 0.03 Hz (current in CED is 6000 A, CED radius is 1000 m); (c) ratios of calculated MT-signals $\varepsilon_{\mathrm{CED}}^{\mathrm{MT}}$ to useful signal $\varepsilon_{\mathrm{CED}}^{\mathrm{HED}}$ in CED receivers with radius of 1000 m for two frequencies: 0.3 Hz and 0.03 Hz (current in HED is 750 A, HED length is 1000 m)

These differences can be decreased by increasing the current in the CED. In the VED/VEL technology the current of 6000 A was set in one line, but in the CED/HEL technology the current of 6000 A in the CED can be obtained at the current 6000/8 = 750 A in each CED wire, and if the current in each CED wire is increased by an order, then the MT-noise/signal ratio for the CED/HEL technology in geoelectrical conditions considered in our paper will become deteriorated only by one order in comparison with the VED/VEL technology that was used in the geoelectrical conditions (at fairly high latitudes, at 70°N) presented in Helwig et al. (2013).

Note again that we do not know the real level of MT-noise; we have obtained only the upper estimate that can be much higher than the real one. Actually, the level of MT-field can be much lower. But, if the level of MT-field appears to be close to our upper estimate, and power consumption by the CED with the current increased for overcoming the MT-noise impact is high, instead of the CED/HEL technology under consideration, another variant of this technology can be used. We will call this variant HED/CED technology. In the HED/CED technology the HED is used as a transmitter and the CED (consisting of 8 radial lines) is used as a receiver. In fact, all the examples studied in Section 3 and the first example in Section 4 correspond to this technology.

Fig. 15c shows the ratios of the calculated MT-signals $\varepsilon_{\mathrm{CED}}^{\mathrm{MT}}$ to the useful signal $\varepsilon_{\mathrm{CED}}^{\mathrm{HED}}$ in CED receivers (with the radius of 1000 m) at 750 A current in the HED of 1000 m in length (in this case the useful signals are just the same as the signals obtained by the CED/HEL technology at 6000 A current in the CED). As seen from Fig. 15c, the MT-noise/signal ratio is the same as for the VED/VEL technology in geoelectrical conditions considered in Helwig et al. (2013). Moreover, there is a possibility to increase the current in the HED, which not only allows the increase of the useful signal but also the improvement of the MT-noise/signal ratio.

Now, we analyze how the random noises can impact the inversions results. We consider the geoelectrical model and the CED system shown in Fig. 10a (note that the performed analysis holds both for CED/HEL technology and for HED/CED technology). The random error added to the synthesized data attains 10% of the useful signal at the time instant 20 s, and its relatively value smoothly decreases with time decreasing (the absolute value of the random error increases with time decreasing but more slowly than the value of the useful signal increases). The 2-D inversion of these synthesized data with noise was performed. Its results are shown in Fig. 16. The comparison of these results with the results of 2-D inversion of the synthesized data without random noise shows that the random noise in data scarcely changes the geoelectrical model obtained as the result of the inversion. Consequently, the signals caused by the objects recovered using "clear" (without noise) and noisy data scarcely differ from each other.

Finally, we estimate the possible influence of ice thickness changing on target detectability. To do this, we include a high resistivity object (simulating a very big ice accretion) under the CED and ice (on which the CED is placed). This object (ice-object) has 500 m in length, 500 m in width and 10 m in thickness. The epicenter of this ice-object is 450 m from the CED center.

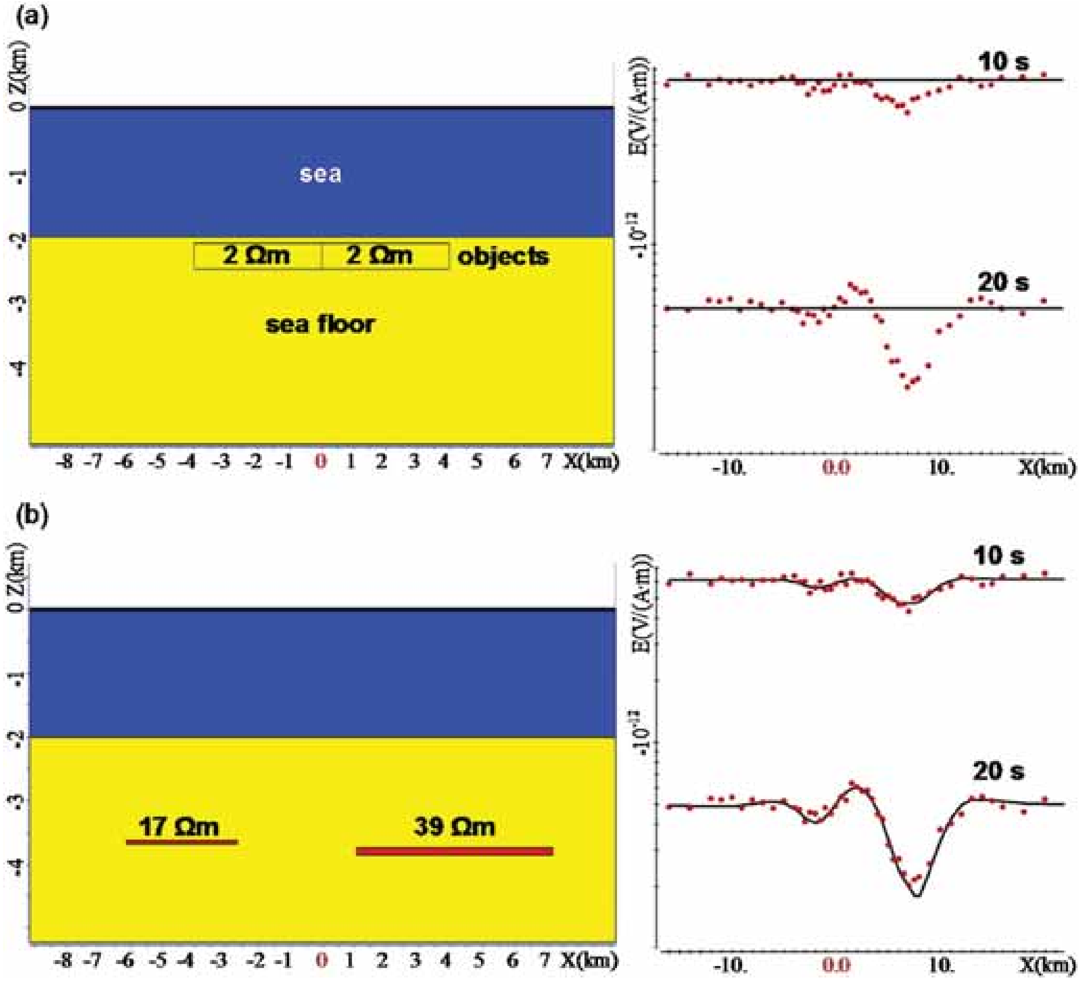

Fig. 16. 2-D inversion of synthetic data (generated by using 3-D model in Fig. 8) with noise. (a) Initial model; (b) final model. The curves in the right represent the generated 3-D data (red points) with noise and forward responses for the model in the left (solid curves) at two measurement times of 10 s and 20 s.

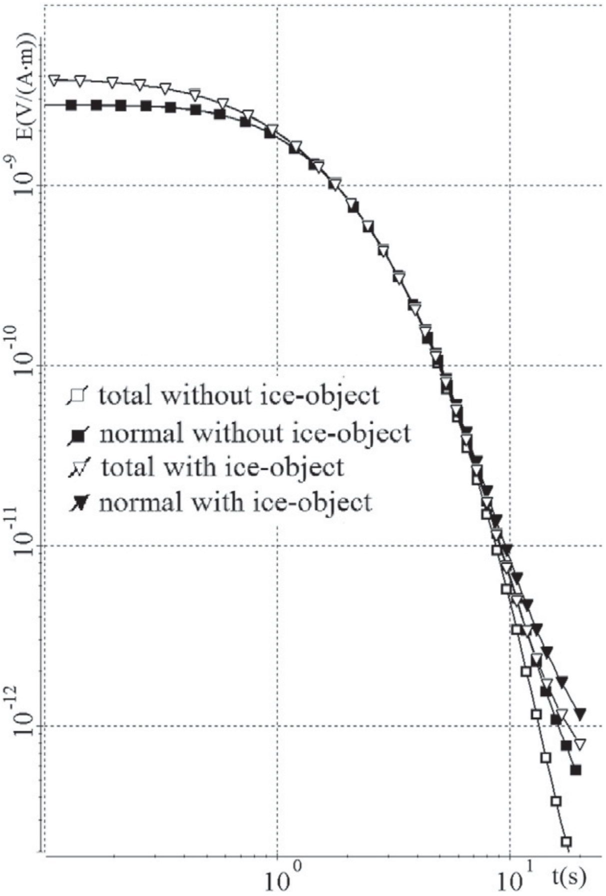

Fig. 17. CED transient responses for the model shown in Fig. 4a and for this model with the ice-object included. CED is located above the middle of the target. The CED radius is 1 km, and the offset from the center is 2 km. "Total without ice-object" stands for the response including target; "normal without ice-object" stands for the background response; "total with ice-object" stands for the response including target and ice-object; "normal with ice-object" stands for the background response that includes ice-object.

The signal (when the CED system is over the target) is shown in Fig. 17. Note that although at the latest times the ice-object causes the change (increase) of the registered signal, but the corresponding signal additives for the geoelectrical model with and without a target are almost equal. Thus, the target identification will be quite possible; it is necessary only to change the normal field of the 1-D background medium for the normal field of medium with the corresponding ice-object(s).

7. Discussion

Application of existing controlled source geoelectric and geoelectromagnetic methods in high latitude Arctic regions has either great difficulty or is generally impossible. In addition to remoteness and harsh weather conditions, which complicate any geophysical operations, the existence of the permanent ice cover particularly affects existing conventional methods. Indeed, the available high resolution marine EM methods, such as CSEM and TEMP-VEL, would need to operate at large depths below the ice that represents severe physical obstacle for their application. On the other hand, conventional surface methods, such as ERT, LOTEM, CSAMT, would be greatly affected by the conductive ocean and sub-bottom sediments, which significantly reduce relative target response of underlying resistive structures and increase necessary offsets to achieve exploration depth required for hydrocarbon or mineral exploration. Such very long offsets inevitably reduce lateral resolution of the methods and could be generally inapplicable in the Arctic Ocean due to the limited size of ice floes, especially during summer time, when they are shrunk to less than 2–3 km in diameter.

The abovementioned conditions, which complicate conventional methods, can be particularly suitable for the proposed ice-borne marine CED method. Indeed, drifting ice floes represent stable platforms for both deployment and relocating the CED transmitter, while the underlying ocean water provides ideal conditions for grounding the CED electrodes. Thus, the operation of the CED system on drifting ice floes may deliver two-fold benefits. First, the method could be applied in areas practically inaccessible to other existing controlled source GE/GEM methods. Second, the use of drifting ice floes facilitates the most efficient moving transmitter sounding mode of operation, which is not otherwise realistic on land and offshore.

8. Conclusions

Despite the lack of field data, preliminary conclusions can be drawn from modeling and general physical considerations.

Placing CED transmitter and receiver electrodes close to the sea bottom insignificantly increases signal detectability, but causes much greater technical difficulties. Therefore the rigid attachment of electrodes to the bottom of the ice floe seems preferable.

Profiling response at late times using the moving CED transmitter-receiver array delineates edges of horizontal resistive targets in situ, prior to applying the complicated multi-dimensional inversions. It provides fairly good lateral resolution with regard to target dimensions as well as for separating different objects from each other.

The proposed simplified 2-D and 3-D inversions using fixed geoelectric parameters of 1-D background medium provide sufficiently accurate quantitative estimates of dimensions and spatial location of parallelepiped targets aligned with the profile. The resistivity of the targets is significantly underestimated.

In case of the considered geometrically simple objects (parallelepipeds), 3-D inversion only marginally improves 2-D inversion, but significantly complicates data acquisition.

At very late times, the CED signal becomes vulnerable to asymmetric locations of electrodes and to current imbalance in different legs. However this problem can be addressed using existing differential GPS and current stabilizators.

A critical experiment to measure electric field noise levels should be undertaken through the ice as a key to feasibility before any attempt is made to assess actual feasibility or design transmitter hardware.

Acknowledgements

The study was performed with the financial support of the Ministry of Education and Science of the Russian Federation under the state task no. 298 and the president grant no. MD-7244.2015.5.

We are grateful to James Macnae for highly useful recommendations and discussion.

References

Constable, S., Srnka, L.J., 2007. An introduction to marine controlled source electromagnetic methods for hydrocarbon exploration. Geophysics 72, WA3–WA12.

Druskin, V.L., Knizhnerman, L.A., 1988. A spectral semi-discrete method for the numerical solution of three-dimensional nonstationary electrical prospecting problems. Izv. Phys. Solid Earth 8, 63–74.

Goldman, M., Mogilatov, V., Haroon, A., Levi, E., Tezkan, B., 2015. Signal detectability of marine electromagnetic methods in the exploration of resistive targets. Geophys. Prospect. 63, 192–210.

Haroon, A., Tezkan, B., Goldman, M., 2014. Development of the marine circular electric dipole method to investigate resistive bodies in shallow marine environments. Extended Abstract, 22nd EM Workshop, Weimar, Germany.

Helwig, S.L., El Kaffas, A.W., Holten, T., Frafjord, O., Eide, K., 2013. Vertical dipole CSEM: technology advances and results from Snohvit field. First Break 31 (4), 63–68.

Holten, T., Flekkøy, E.G., Måløy, K.J., Singer, B., 2009. Vertical source and receiver CSEM method in time-domain. SEG Annual Meeting, Houston, Texas, Expanded Abstracts, pp. 749–752.

Jokat, W., 2005. The sedimentary structure of the Lomonosov Ridge between 88° N and 80° N. Geophys. J. Int. 163 (2), 698–726.
Mogilatov, V., 1992. A circular electric dipole as a new source in electric surveys. Izv. Phys. Solid Earth 6, 97–105.
Mogilatov, V., Balashov, B., 1996. A new method of geoelectrical prospecting by vertical electric current soundings. J. Appl. Geophys. 36, 31–41.
Persova, M.G., Soloveichik, Y.G., Trigubovich, G.M., 2011. Computer modeling of geoelectromagnetic fields in three-dimensional media by the finite element method. Izv. Phys. Solid Earth 47 (2), 79–89. http://dx.doi.org/10.1134/S1069351311010095.
Persova, M.G., Soloveichik, Y.G., Trigubovich, G.M., Tokareva, M.G., 2013. Methods and algorithms for reconstructing three-dimensional distributions of electric conductivity and polarization in the medium by finite-element 3D modeling using the data of electromagnetic sounding. Izv. Phys. Solid Earth 49 (3), 329–343. http://dx.doi.org/10.1134/S1069351313030117.
Poselov, V.A., Avetisov, G.P., Butsenko, V.V., Zholondz, S.M., Kaminsky, V.D., Pavlov, S.P., 2012. The Lomonosov Ridge as a natural extension of the Eurasian continental margin into the Arctic Basin. Russ. Geol. Geophys. 53, 1276–1290.
Trofimov, I.L., Fonarev, G.A., 1976. Deep magnetotelluric surveys in theArctic Ocean. Geoelectric Geotherm. Stud. 712–715.
Weber, J.R., 1983. Maps of the Arctic Ocean sea floor: a history of bathymetry and its interpretation. Geological Survey of Canada, Open File 2009, pp. 85–106.